GSA DATA REPOSITORY 2014283

Strontium isotope stratigraphy from the Early Triassic of Zal, Iran: Linking temperature to weathering rates and the tempo of ecosystem recovery

Alexa R. C. Sedlacek, Matthew R. Saltzman, Thomas J. Algeo, Micha Horacek, Rainer Brandner, Kenneth Foland, and Rhawn F. Denniston

Paleogeography of Zal Section

The study section is located in northwestern Iran, 30 km south of Julfa, near the village of Zal (N38°43′47″, E45°36′13″, 1600 m; Fig. 1). The section accumulated as a carbonate platform succession on the Iranian microcontinent during the Early Triassic (Fig. DR1; Sengör, 1984; Besse et al., 1998). The Iranian microcontinent formed part of the Cimmeria terranes separating the Neotethys and Paleotethys oceans (Sengör, 1984; see Fig. DR1). The section represents relatively continuous deposition without evidence of major intraformational hiati (Horacek et al., 2007). The Dienerian is represented by nearly 300 m of strata (Fig. 2), enabling high-resolution sampling through this substage.

Biostratigraphy of Zal Section

Stage and substage boundaries at Zal are based on Horacek et al. (2007). The Permian-Triassic boundary (PTB) and Griesbachian substage are biostratigraphically well constrained: *Hindeodus parvus* has been reported at 0.7 m, and *Isarcicella isarcica* from 3.5 m and 11 m (Horacek et al., 2007; Richoz et al., 2010). The bivalve *Claraia* dominates the upper Griesbachian beds, and the base of the Dienerian has been placed near the top of the *Claraia*-rich interval. This placement is consistent with the of the Griesbachian-Dienerian boundary at the Abadeh section in central Iran, which contains more diagnostic fossils near the base of the Dienerian. The overlying strata are less well-constrained biostratigraphically, and substage assignments were made on the basis of a combination of index fossils and carbon isotope stratigraphy (i.e., $\delta^{13}C$ correlations with well-dated sections elsewhere in the Tethys) (Horacek et al., 2007). The Dienerian-Smithian boundary is marked by a pronounced positive $\delta^{13}C_{carb}$ excursion. Below the peak of this excursion, Horacek et al. (2007) reported *Neogondolella dieneri*, which confirms the Dienerian age of these strata. The presence of *Pachycladina* at 570 m indicates a Smithian age. Placement of the Smithian/Spathian boundary is based on correlation with existing C isotope curves from other biostratigraphically well-constrained sections. Its position above the last *Hadrodontina* conodonts is consistent with other Iranian Early Triassic sections (Horacek et al., 2007).

Early Triassic Time Scale and Sedimentation Rates

The timescale used in this study differs from the ages in the Geologic Time Scale 2012 (Gradstein et al., 2012). We elected to follow the timescale presented by Algeo et al. (2013), which is in better agreement with radiometric age dates for the base of the Smithian and Spathian substages published by Galfetti et al. (2007) and Ovtcharova et al. (2006), respectively. However, we modified this timescale to reflect revised estimates of the durations of the

Griesbachian and Dienerian substages based on astronomical tuning of magnetic susceptibility data by Wu et al. (2012). This adjustment resulted in a shorter Griesbachian (0.50 Myr versus 0.7 Myr) and a longer Dienerian (0.62 Myr versus 0.4 Myr) relative to the Algeo et al. (2013) timescale. The revised timescale is given in Table DR2. It is possible that future revisions of the Early Triassic timescale will necessitate modifications to the rates of $^{87}Sr/^{86}Sr$ change calculated below.

The Lower Triassic at Zal comprises ~125 m of Griesbachian strata, ~375 m of Dienerian strata, ~100 m of Smithian strata, and ~130 m of Spathian strata. Given estimated durations of 500 kyr, 620 kyr, 400 kyr, and 3,450 kyr for these four substages of the Early Triassic (Table S

DR2), the corresponding average sedimentation rates are 250 m m.y.$^{-1}$, 605 m m.y.$^{-1}$, 250 m m.y.$^{-1}$, and 38 m m.y.$^{-1}$, respectively. The Griesbachian through Smithian values are substantially elevated compared to average long-term cratonic sedimentation rates (~30 m m.y.$^{-1}$; Sadler, 1981; Anders et al., 1987), but the Spathian estimate is not exceptional. The unusually high sedimentation rates that prevailed during the Griesbachian through Smithian may be a reflection of intensified subaerial weathering and elevated fluxes of both dissolved and particulate erosional products to the global ocean during the first ~1.6 m.y. of the Early Triassic (Algeo and Twitchett, 2010). It should be noted that this pattern of secular variation in sedimentation rates is consistent with patterns of weathering rate changes based on modeled riverine Sr fluxes (Fig. 3B), despite being based on completely independent proxies (i.e., stratal thickness versus carbonate $^{87}Sr/^{86}Sr$ ratios).

$^{87}Sr/^{86}Sr$ Data and Diagenetic Influences

Sr concentrations and $^{87}Sr/^{86}Sr$ ratios for the study samples are given in Table DR1. The samples are the same as those used in the carbon isotope study of Horacek et al. (2007).

Because diagenetic alteration typically depletes the Sr concentration of carbonate marine sediments, samples with higher Sr concentrations are likely to represent greater initial Sr concentrations, and the $^{87}Sr/^{86}Sr$ of these samples is less susceptible to alteration (Brand and Veizer, 1980; Denison et al., 1994a). The relatively high concentrations of Sr in most samples increase our confidence that the $^{87}Sr/^{86}Sr$ ratios from Zal represent primary Early Triassic seawater values (Fig. DR2). Diagenesis generally alters $^{87}Sr/^{86}Sr$ toward higher values due to exchange with clay minerals enriched in ^{87}Sr, although Sr exchange with igneous sills can potentially lower $^{87}Sr/^{86}Sr$ (Veizer and Compston, 1974). In the study section, two Griesbachian-age samples associated with sills exhibit ^{87}Sr enrichment, and we consider these samples to be altered (Fig. 2, Fig. DR2).

Seawater Sr Isotope Model Design

The Sr isotopic composition of seawater can be modeled using a standard reservoir (or box) modeling approach. Changes in the Sr-isotopic composition of seawater ($\delta^{87}Sr$) from *t* to *t+1* were calculated as:

$$\delta^{87}Sr_{(t+1)} = (M_{Sr(t)} \cdot \delta^{87}Sr_{(t)} + \Sigma(\int_t^{t+1} \delta_i \cdot f_i)) / (M_{Sr\,(t)} + \Sigma(\int_t^{t+1} f_i)) \quad (1)$$

Equation 1 is an expression of isotopic mass balance where $M_{Sr(t)}$ is the mass of seawater Sr at time t, δ_i is the isotopic composition of source i, and f_i is the flux of source i. The model incorporates three source fluxes (see below) and assumes no fractionation of Sr isotopes during removal of Sr from seawater, making a sink flux term unnecessary. The LOWESS curve for smoothing of data in high-data-density intervals was generated using the algorithm presented in Algeo et al. (2014) and Song et al. (2014), and the spline function used in low-data-density intervals was generated in MATLAB. Model output is given in Table DR3.

Model parameterization was based on studies of the modern and ancient marine Sr cycle. The total mass of Sr in seawater is 1.25×10^{17} mol (Richter and Turekian, 1993). The main inputs to seawater Sr are the (1) riverine flux, (2) ocean-crustal hydrothermal flux, and (3) marine diagenetic carbonate flux. Studies of the modern Sr cycle have shown that the riverine flux is enriched in the heavy (or radiogenic) isotope of Sr (^{87}Sr) as a consequence of weathering of old crystalline terrains in which large amounts of ^{87}Rb have decayed. The average global $^{87}Sr/^{86}Sr$ ratio of rivers is ~0.712, although individual rivers can yield $^{87}Sr/^{86}Sr$ ratios ranging from at least 0.705 to nearly 0.800 (Wadleigh et al., 1985; Palmer and Edmond, 1989; Krishnaswami et al., 1992). In contrast, the hydrothermal flux is enriched in the light (or non-radiogenic) isotope of Sr (^{86}Sr) owing to its origin in young, Rb-poor oceanic crust. This flux has a nearly uniform $^{87}Sr/^{86}Sr$ ratio of ~0.703 (Albarède et al., 1981). The diagenetic carbonate flux represents interaction of seawater with marine sedimentary carbonates (Richter and Liang, 1993). Since the latter record the Sr isotopic composition of seawater, this flux has had intermediate compositions through the Phanerozoic (~0.707-0.709; McArthur et al., 2001). For the modern Sr cycle, the riverine, hydrothermal, and diagenetic carbonate fluxes have been estimated at ~3.3, 1.0, and 0.3×10^{10} mol y^{-1}, respectively (Richter and Turekian, 1993).

Sr is removed from seawater as a component of marine carbonates and evaporites and, to a limited degree, in ocean-crustal reactions. The relative magnitudes of these sink fluxes are unimportant, however, because of lack of fractionation among them (Albarède et al., 1981). For this reason, the Sr isotopic composition of seawater can be modeled simply as a mass balance among its source fluxes. Our model assumes that the seawater Sr cycle is in equilibrium at all times such that the source fluxes of Sr are balanced by the sink fluxes.

Because there are three source fluxes of Sr to seawater, each with its own $^{87}Sr/^{86}Sr$ ratio, the model is underconstrained when marine carbonate $^{87}Sr/^{86}Sr$ ratios are used as the sole input. Our model makes use of a simplified approach in which the fluxes and isotopic compositions for the hydrothermal and diagenetic carbonate sources are assumed to be invariant: (1) 2.0×10^{10} mol y^{-1} and 0.703 $^{87}Sr/^{86}Sr$ for the hydrothermal flux, and (2) 0.3×10^{10} mol y^{-1} and 0.7084 $^{87}Sr/^{86}Sr$ for the diagenetic carbonate flux. We adopted a higher value for the hydrothermal flux (2.0×10^{10} mol y^{-1}) than in the modern (1.0×10^{10} mol y^{-1}) owing to generally higher eustatic elevations (Algeo and Seslavinsky, 1995; Haq and Schutter, 2008) and, thus, inferred higher ocean-crustal spreading rates in the Late Paleozoic (Gaffin, 1987). The isotopic composition chosen for the diagenetic carbonate flux (0.7084 $^{87}Sr/^{86}Sr$; Richter and Turekian, 1993) represents an average value for Paleozoic marine carbonates, i.e., the sediments that would have been actively undergoing isotopic exchange with seawater at the PTB (Denison et al., 1994b). In

fact, the model is relatively insensitive to variations in these four parameters, which can vary over any range of reasonable values without greatly affecting the model results.

The parameterization of the model was designed to achieve an initial equilibrium seawater $^{87}Sr/^{86}Sr$ ratio of 0.70705, which is close to the observed value of ~0.70707 for latest Permian carbonates at Zal (Table DR1). The relatively low $^{87}Sr/^{86}Sr$ ratio of latest Permian seawater requires that one or more of the source fluxes of Sr differed considerably from that in the modern ocean, in which seawater $^{87}Sr/^{86}Sr$ is 0.70925 (Richter and Turekian, 1993). Lower seawater $^{87}Sr/^{86}Sr$ ratios can be achieved through higher hydrothermal fluxes, lower riverine fluxes, or reduced riverine $^{87}Sr/^{86}Sr$. We chose to model the system with elevated hydrothermal fluxes, which has the advantage of not systemically skewing riverine fluxes or $^{87}Sr/^{86}Sr$ ratios high or low relative to their modern values. However, we do not know with certainty which of these factors was primarily responsible for low Late Permian seawater $^{87}Sr/^{86}Sr$ ratios. In the context of model output, the initial parameterization is of limited significance, because all reasonable combinations yield the same general patterns of secular variation in riverine fluxes and $^{87}Sr/^{86}Sr$ ratios (e.g., Fig. 3B).

Seawater Sr Isotope Model Results

Because model output is relatively insensitive to variations in the flux and Sr-isotopic composition of the ocean-crust hydrothermal and marine-carbonate diagenetic sources, the most important influences on secular variation of seawater $^{87}Sr/^{86}Sr$ are (1) the Sr isotopic composition of the riverine flux, and (2) the ratio of the riverine and hydrothermal fluxes (cf. Hodell et al., 1990; Goddéris and François, 1995). In essence, the system consists of two unknowns that are constrained by a single input, i.e., measured marine carbonate $^{87}Sr/^{86}Sr$ ratios. We therefore investigated two scenarios, one in which the Sr isotopic composition of the riverine flux was held constant and the ratio of the riverine and hydrothermal fluxes was allowed to vary (Scenario 1; Fig. 3B, F_{RIV}), and a second in which the ratio of the riverine and hydrothermal fluxes was held constant and the Sr isotopic composition of the riverine flux was allowed to vary (Scenario 2; Fig. 3B, $^{87}Sr/^{86}Sr$). See the main text for a discussion of the results of these two scenarios.

Variations in Phanerozoic seawater $^{87}Sr/^{86}Sr$ have been attributed to changes in both the flux and the isotopic composition of riverine Sr. Derry and France-Lanord (1996) calculated that the rise in seawater $^{87}Sr/^{86}Sr$ from ~0.7089 in the late Miocene to ~0.7092 today could have been achieved by an increase in the Sr flux of the Ganges-Brahmaputra river system by a factor somewhat greater than two. Hodell et al. (1990) calculated that the same rise could have been achieved by an increase in the global riverine Sr flux of ~25%. These values are modest compared to the inferred nearly 3x increase in riverine Sr flux that would be necessary to account for the rapid rise in Early Triassic seawater $^{87}Sr/^{86}Sr$ (Fig. 3B). However, the latter estimate is not unreasonable in view of evidence of widespread intensified subaerial erosion following the end-Permian crisis (Ward et al., 2000; Retallack, 2005; Sephton et al., 2005; see review in Algeo et al., 2011). Indeed, a 3x increase in riverine Sr flux is similar to the 4x increase in global marine siliciclastic sedimentation rates during the Early Triassic estimated by Algeo et al. (2011; n.b., revised from the original 7x estimate of Algeo and Twitchett, 2010).

The range of modeled riverine Sr fluxes for the Early Triassic (~1.7 to 5.3 x 10^{10} mol yr^{-1}; Fig. 3B) brackets the modern flux (3.3 x 10^{10} mol yr^{-1}; Richter and Turekian, 1993). This

range is reasonable given multiple competing influences on Early Triassic riverine Sr fluxes: (1) warmer climatic conditions leading to intensified chemical weathering and, thus, higher Sr fluxes (Algeo et al., 2011; Retallack et al., 2011), and (2) the existence of a single large continent (Pangea) having extensive areas of internal drainage, reducing the effective land area contributing riverine Sr to the ocean and, thus, lower Sr fluxes (cf. Gibbs et al., 1999). A different initial parameterization of riverine Sr flux would yield a lower or higher range of absolute values for the model output but with little or no change in the pattern of secular variation. The model results are thus robust with regard to general patterns of variation in the modeled parameters.

The second possibility, that the Early Triassic rise in seawater $^{87}Sr/^{86}Sr$ was due to an increase in riverine $^{87}Sr/^{86}Sr$ ratios, is perhaps less plausible. Hodell et al. (1990) calculated that the rise in seawater $^{87}Sr/^{86}Sr$ since the late Miocene could have been achieved by an increase in the riverine $^{87}Sr/^{86}Sr$ ratio of just 0.0006, which is approximately an order of magnitude less than the 0.005 increase in riverine $^{87}Sr/^{86}Sr$ we calculated for the Early Triassic (Fig. 3B). The difference is that the Miocene-to-Recent rise occurred over a time interval (8 m.y.) far longer than that for the Early Triassic (<5 m.y.). Although the Sr isotopic composition of individual river systems is known to have varied temporally, e.g., from <0.72 to >0.74 for the Ganges-Brahmaputra system over the past 7 m.y. (Derry and France-Lanord, 1996), it is unknown whether the global riverine Sr flux could exhibit similarly large fluctuations. In any case, such fluctuations are typically attributed to orogenic uplift and exposure of old sedimentary and crystalline rocks (Richter et al., 1992), whereas the Early Triassic is not a known interval of major orogeny. Rather, the timing of changes in the seawater Sr isotope record appears closely related to major environmental perturbations of latest Permian to mid-Early Triassic age and to consequent changes in subaerial weathering rates (Algeo et al., 2011).

References

Albarède, F., Michard, A., Minster, J.F., and Michard, G., 1981, $^{87}Sr/^{86}Sr$ ratios in hydrothermal waters and deposits from the East Pacific Rise at 21°N: Earth and Planetary Science Letters, v. 55, p. 229-236.

Algeo, T.J., and Seslavinsky, K.B., 1995, The Paleozoic world: continental flooding, hypsometry, and sea level: American Journal of Science, v. 295, p. 787-822.

Algeo, T.J., and Twitchett, R.J., 2010, Anomalous Early Triassic sediment fluxes due to elevated weathering rates and their biological consequences: Geology, v. 38, p. 1023-1026.

Algeo, T.J., Chen, Z.Q., Fraiser, M.L., and Twitchett, R.J., 2011, Terrestrial-marine teleconnections in the collapse and rebuilding of Early Triassic marine ecosystems: Palaeogeography, Palaeoclimatology, Palaeoecology, v. 308, p. 1-11.

Algeo, T.J., Henderson, C.M., Tong, J., Feng, Q., Yin, H., and Tyson, R.V., 2013, Plankton and productivity during the Permian-Triassic boundary crisis: An analysis of organic carbon fluxes: Global and Planetary Change, v. 105, p. 52-67.

Algeo, T.J., Meyers, P.A., Robinson, R.S., Rowe, H., and Jiang, G., 2014, Icehouse-greenhouse variations in marine denitrification: Biogeosciences, v. 11, p. 1273-1295.

Anders, M.H., Krueger, S.W., and Sadler, P.M., 1987, A new look at sedimentation rates and completeness of the stratigraphic record: Journal of Geology, v. 95, p. 1-14.

Besse, J., Torq, F., Gallet, Y., Ricou, L.E., Krystyn, L., and Saidi, A., 1998, Late Permian to Late Triassic paleomagnetic data from Iran: constraints on the migration of the Iranian block through the Tethyan Ocean and initial destruction of Pangaea: Geophysical Journal International, v. 135, p. 77–92.

Brand, U., and Veizer, J., 1980, Chemical diagenesis of a multicomponent carbonate system-1: trace elements: Chemical Geology, v. 50, p. 1219-1236.

Denison, R.E., Koepnick, R.B., Fletcher, A., Howell, M.W., and Callaway, W.S., 1994a, Criteria for the retention of original seawater $^{87}Sr/^{86}Sr$ in ancient shelf limestones: Chemical Geology, v. 112, p. 131-143.

Denison, R.E., Koepnick, R.B., Burke, W.H., Hetherington, E.A., and Fletcher, A., 1994b, Construction of the Mississippian, Pennsylvanian and Permian seawater $^{87}Sr/^{86}Sr$ curve: Chemical Geology, v. 112, p. 145-167.

Derry, L.A., and France-Lanord, C., 1996, Neogene Himalayan weathering history and river $^{87}Sr/^{86}Sr$: impact on the marine Sr record: Earth and Planetary Science Letters, v. 142, p. 59-74.

Gaffin, S., 1987, Ridge volume dependence on seafloor generation rate and inversion using long-term sealevel change: American Journal of Science, v. 287, p. 596-611.

Galfetti, T., Bucher, H., Ovtcharova, M., Schaltegger, U., Brayard, A., Brühwiler, T., Goudemand, N., Weissert, H., Hochuli, P.A., Cordey, F., and Guodun, K., 2007, Timing of the Early Triassic carbon cycle perturbations inferred from new U-Pb ages and ammonoid biochronozones: Earth and Planetary Science Letters, v. 258, p. 593-604.

Gibbs, M.T., Bluth, G.J.S., Fawcett, P.J., and Kump, L.R., 1999, Global chemical erosion over the last 250 my: variations due to changes in paleogeography, paleoclimate, and paleogeology: American Journal of Science, v. 299, p. 611-651.

Goddéris, Y., and François, L.M., 1995, The Cenozoic evolution of the strontium and carbon cycles: relative importance of continental erosion and mantle exchanges: Chemical Geology, v. 126, p. 169-190.

Gradstein, F.M., Ogg, J.G., Schmitz, M., and Ogg, G., eds., 2012, The Geologic Time Scale 2012. Boston, MA, Elsevier, 1176 pp.

Haq, B.U., and Schutter, S.R., 2008, A chronology of Paleozoic sea-level changes: Science, v. 322, p. 64-68.

Hodell, D.A., Mead, G.A., and Mueller, P.A., 1990, Variation in the strontium isotopic composition of seawater (8 Ma to present): implications for chemical weathering rates and dissolved fluxes to the oceans: Chemical Geology, v. 80, p. 291-307.

Horacek, M., Richoz, S., Brandner, R., Krystyn, L., and Spötl, C., 2007, Evidence for recurrent changes in Lower Triassic oceanic circulation of the Tethys: The $\delta^{13}C$ record from marine sections in Iran: Palaeogeography, Palaeoclimatology, Palaeoecology, v. 252, p. 355-369.

Krishnaswami, S., Trivedi, J.R., Sarin, M.M., Ramesh, R., and Sharma, K.K., 1992, Strontium isotopes and rubidium in the Ganga-Brahmaputra river system: weathering in the Himalaya, fluxes to the Bay of Bengal and contributions to the evolution of oceanic $^{87}Sr/^{86}Sr$: Earth and Planetary Science Letters, v. 109, p. 243-253.

Lehrmann, D.J., Ramezani, J., Bowring, S.A., Martin, M.W., Montgomery, P., Enos, P., Payne, J.L., Orchard, M.J., Wang, H.M., and Wei, J.Y., 2006, Timing of recovery from the end-Permian extinction: Geochronologic and biostratigraphic constraints from south China: Geology, v. 34, p. 1053-1056.

McArthur, J.M., Howarth, R.J., and Bailey, R.R., 2001, Strontium isotope stratigraphy: LOWESS version 3: best fit to the marine Sr-isotope curve for 0-509 Ma and accompanying look-up table for deriving numerical age: Journal of Geology, v. 109, p. 155-170.

Ovtcharova, M., Bucher, H., Schaltegger, U., Galfetti, T., Brayard, A., and Guex, J., 2006, New Early to Middle Triassic U-Pb ages from South China: Calibration with ammonoid biochronozones and implications for the timing of the Triassic biotic recovery: Earth and Planetary Science Letters, v. 243, p. 463-475.

Palmer, M.R., and Edmond, J.M., 1989, The strontium isotope budget of the modern ocean: Earth and Planetary Science Letters, v. 92, p. 11-26.

Retallack, G.J., 2005, Earliest Triassic claystone breccias and soil-erosion crisis: Journal of Sedimentary Research, v. 75, p. 679-695.

Retallack, G.J., Sheldon, N.D., Carr, P.F., Fanning, M., Thompson, C.A., Williams, M.L., Jones, B.G., and Hutton, A., 2011, Multiple Early Triassic greenhouse crises impeded recovery from Late Permian mass extinction: Palaeogeography, Palaeoclimatology, Palaeoecology, v. 308, p. 233-251.

Richter, F.M., and Liang, Y., 1993, The rate and consequences of Sr diagenesis in deep-sea carbonates: Earth and Planetary Science Letters, v. 117, p. 553-565.

Richter, F.M., and Turekian, K.K., 1993, Simple models for the geochemical response of the ocean to climatic and tectonic forcing: Earth and Planetary Science Letters, v. 119, p. 121-131.

Richter, F.M., Rowley, D.B., and DePaolo, D.J., 1992, Sr isotope evolution of seawater: the role of tectonics: Earth and Planetary Science Letters, v. 109, p. 11-23.

Richoz, S., Leopold, K., Baud, A., Brandner, R., Horacek, M., and Mohtat-Aghai, P., 2010, Permian-Triassic boundary interval in the Middle East (Iran and N. Oman): Progressive environmental change from detailed carbonate carbon isotope marine curve and sedimentary evolution: Journal of Asian Earth Sciences, v. 39, p. 236-253.

Sadler, P.M., 1981, Sediment accumulation rates and the completeness of stratigraphic sections: Journal of Geology, v. 89, p. 569-584.

Sengör, A.M.C., 1984, The Cimmeride Orogenic System and the tectonics of Eurasia: Geological Society of America Special Paper 195, 82 pp.

Sephton, M.A., Looy, C.V., Brinkhuis, H., Wignall, P.B., de Leeuw, J.W., and Visscher, H., 2005, Catastrophic soil erosion during the end-Permian biotic crisis: Geology, v. 33, p. 941-944.

Shen, S.Z., and 21 coauthors, 2011, Calibrating the end-Permian mass extinction: Science, v. 334, p. 1367-1372.

Song, H.Y., Tong, J., Algeo, T.J., Song, H.J., Qiu, H., Zhu, Y., Tian, L., Bates, S., Lyons, T.W., Luo, G., and Kump, L., 2014, Early Triassic seawater sulfate drawdown: Geochimica et Cosmochimica Acta, v. 128, p. 95-113.

Veizer, J., and Compston, W., 1974, $^{87}Sr/^{86}Sr$ composition of seawater during the Phanerozoic: Geochimica et Cosmochimica Acta, v. 38, p. 1461-1484.

Wadleigh, M.A., Veizer, J., and Brooks, C., 1985, Strontium and its isotopes in Canadian rivers: fluxes and global implications: Geochimica et Cosmochimica Acta, v. 49, p. 1727-1736.

Ward, P.D., Montgomery, D.R., and Smith, R., 2000, Altered river morphology in South Africa related to the Permian-Triassic extinctions: Science, v. 289, p. 1740-1743.

Wu, H., Zhang, S., Feng, Q., Jiang, G., Li, H., and Yang, T., 2012, Milankovitch and sub-Milankovitch cycles of the early Triassic Daye Formation, South China and their geochronological and paleoclimatic implications: Gondwana Research, v. 22, p. 748-759.
Zhao, L.S., Orchard, M.J., Tong, J.N., Sun, Z.M., Zuo, J.X., Zhang, S.X., and Yun, A.L., 2007, Lower Triassic conodont sequence in Chaohu, Anhui Province, China and its global correlation: Palaeogeography, Palaeoclimatology, Palaeoecology, v. 252, p. 24-38.

Table DR1: $^{87}Sr/^{86}Sr$ results for the latest Permian through Early Triassic of Zal, Iran

Sample name	Height (m)	Sr (ppm)	$^{87}Sr/^{86}Sr$	uncertainty	(Sub)stage	Age (Ma)
IZ153a	728	31.91	0.708100	0.000012	Spathian	247.280
IZ145	703.2	22.61	0.708128	0.000012	Spathian	247.945
IZ132	645.2	154.12	0.708010	0.000010	Spathian	249.500
IZ131	639.2	145.92	0.707982	0.000011	Spathian	249.661
IZ122	600	263.85	0.707878	0.000010	Spathian	250.658
IZ120	594	303.42	0.707871	0.000090	Smithian	250.678
IZ113	565.7	486.19	0.707862	0.000012	Smithian	250.774
IZ111	554.6	405.03	0.707724	0.000010	Smithian	250.812
IZ108	544.35	517.68	0.707707	0.000009	Smithian	250.847
IZ 104	525.7	563.64	0.707681	0.000010	Smithian	250.910
IZ100	513.6	415.02	0.707737	0.000013	Smithian	250.951
IZ99	512.5	357.66	0.707594	0.000011	Smithian	250.955
IZ98	504.3	356.35	0.707662	0.000014	Smithian	250.983
IZ96	491.5	314.81	0.707590	0.000006	Dienerian	251.014
IZ95	487.5	287.16	0.707585	0.000007	Dienerian	251.021
IS92	474.5	1222.40	0.707548	0.000007	Dienerian	251.044
IS90	467.5	20.84	0.707605	0.000013	Dienerian	251.057
IS86	462.5	559.23	0.707517	0.000009	Dienerian	251.066
IS84	452.5	307.26	0.707524	0.000010	Dienerian	251.084
IS83	447.5	278.13	0.707490	0.000006	Dienerian	251.093
IS82	443.5	468.83	0.707514	0.000010	Dienerian	251.100
IS76	406.5	738.54	0.707473	0.000007	Dienerian	251.166
IS72	389.8	956.42	0.707503	0.000010	Dienerian	251.196
IS69	374.3	578.81	0.707489	0.000008	Dienerian	251.224
IS 67	361.6	1250.53	0.707468	0.000010	Dienerian	251.246
IS 65	348	1189.30	0.707484	0.000008	Dienerian	251.271
IS 64	346	637.78	0.707501	0.000009	Dienerian	251.274
IS63	345.5	573.49	0.707513	0.000021	Dienerian	251.275
IS62	343	1322.08	0.707498	0.000012	Dienerian	251.280
IS61	335.5	831.36	0.707501	0.000009	Dienerian	251.293
IZ60	333	636.85	0.707549	0.000013	Dienerian	251.298
IZ 47	332	1071.98	0.707459	0.000009	Dienerian	251.299
IZ44	315.2	560.58	0.707539	0.000007	Dienerian	251.330
IZ43	314.4	1061.79	0.707467	0.000007	Dienerian	251.331
IZ39	262.15	831.08	0.707427	0.000009	Dienerian	251.425
IZ35	242.6	1905.06	0.707397	0.000008	Dienerian	251.459

IZ34	237.6	592.75	0.707451	0.000009	Dienerian	251.468
IZ32	227.6	947.20	0.707479	0.000013	Dienerian	251.486
IZ29	178	730.00	0.707447	0.000014	Dienerian	251.575
IZ28	170	1046.99	0.707396	0.000008	Dienerian	251.589
IZ27	165	1191.02	0.707386	0.000007	Dienerian	251.598
IZ26	160	1244.84	0.707358	0.000009	Dienerian	251.607
IZ25	155	1387.48	0.707366	0.000016	Dienerian	251.616
IZ24	145	1176.69	0.707401	0.000009	Dienerian	251.634
IZ21	125	181.53	0.707413	0.000017	Dienerian	251.670
IZ20	120	262.85	0.707594	0.000014	Griesbachian	251.690
IZ18	110	585.17	0.707265	0.000008	Griesbachian	251.730
IZ14	45	228.63	0.707645	0.000024	Griesbachian	251.990
IZ11	30	562.11	0.707200	0.000011	Griesbachian	252.050
IZ10	25	317.15	0.707153	0.000009	Griesbachian	252.070
IZ8	15	418.00	0.707217	0.000010	Griesbachian	252.110
IZ6	5	312.07	0.707220	0.000009	Griesbachian	252.150
IZ4	-5	230.63	0.707212	0.000014	Changhsingian	252.190
IZ3	-10	309.88	0.707166	0.000007	Changhsingian	252.210
IZ2	-15	224.80	0.707099	0.000009	Changhsingian	252.230
IZ1	-20	238.57	0.707072	0.000007	Changhsingian	252.250

Table DR2. Late Permian-Middle Triassic time scale

Series	Stage	Substage	Conodont zone	Age of base (Ma)	Duration (Myr)	Radiometric constraints
Mid Tri	Anisian	Aegean		247.2		Lehrmann et al. 2006
Early Tri	Olenekian	Spathian	homeri	250.6	3.40	Ovtcharova et al. 2006
Early Tri	Olenekian	Spathian	pingding.	250.65	0.05	est. Zhao et al. 2007
Early Tri	Olenekian	Smithian	waageni	251.05	0.40	Galfetti et al. 2007
Early Tri	Induan	Dienerian	dieneri	251.42	0.37	Wu et al. 2012
Early Tri	Induan	Dienerian	kummeli	251.67	0.25	Wu et al. 2012
Early Tri	Induan	Griesb.	discreta	251.74	0.07	Wu et al. 2012
Early Tri	Induan	Griesb.	krystyni	251.90	0.16	est. Zhao et al. 2007
Early Tri	Induan	Griesb.	carinata	252.11	0.21	Wu et al. 2012
Early Tri	Induan	Griesb.	isarcica	252.14	0.03	Shen et al. 2011
Early Tri	Induan	Griesb.	parvus	252.17	0.03	Shen et al. 2011
Late Pm	Changhs.		meishanensis	252.28	0.09	Shen et al. 2011
Late Pm	Changhs.		yini	252.32	0.04	Shen et al. 2011
Late Pm	Changhs.		changxing.	253.60	1.28	

Abbreviations: pingding. = pingdingshanensis; changxing. = changxingensis; Griesb. = Griesbachian; Changhs. = Changhsingian

Table DR3: Early Triassic seawater Sr cycle model results

Age	$^{87}Sr/^{86}Sr_{(SW)}$	$^{87}Sr/^{86}Sr_{(RIV)}$	F_{RIV} (10^6 mol y^{-1})
247.25	0.708098	0.710690	2.40
247.35	0.708104	0.710710	2.42
247.45	0.708109	0.710730	2.44
247.55	0.708114	0.710750	2.46
247.65	0.708119	0.710780	2.49
247.75	0.708123	0.710820	2.52
247.85	0.708126	0.710860	2.56
247.95	0.708128	0.710900	2.60
248.05	0.708129	0.710930	2.63
248.15	0.708129	0.710970	2.67
248.25	0.708128	0.711020	2.71
248.35	0.708125	0.711050	2.74
248.45	0.708122	0.711080	2.78
248.55	0.708117	0.711110	2.80
248.65	0.708111	0.711140	2.83
248.75	0.708104	0.711170	2.86
248.85	0.708095	0.711200	2.89
248.95	0.708086	0.711230	2.92
249.05	0.708075	0.711260	2.94
249.15	0.708063	0.711290	2.96
249.25	0.708049	0.711310	2.99
249.35	0.708034	0.711330	3.02
249.45	0.708018	0.711310	3.02
249.55	0.708001	0.711290	3.00
249.65	0.707984	0.711260	2.93
249.75	0.707968	0.711170	2.87
249.85	0.707953	0.711060	2.80
249.95	0.707941	0.711005	2.75
250.05	0.707929	0.710940	2.69
250.15	0.707919	0.710900	2.66
250.25	0.707910	0.710870	2.62
250.35	0.707901	0.710840	2.59
250.45	0.707893	0.710800	2.57
250.55	0.707886	0.710760	2.55
250.65	0.707879	0.712230	3.83
250.75	0.707828	0.714230	5.53
250.85	0.707716	0.712330	3.93
250.95	0.707654	0.713470	4.85

251.05	0.707556	0.711900	3.53
251.15	0.707500	0.710070	2.08
251.25	0.707495	0.709830	1.87
251.35	0.707497	0.711870	3.55
251.45	0.707438	0.710700	2.58
251.55	0.707412	0.710600	2.53
251.65	0.707387	0.709750	1.87
251.65	0.707386	0.713000	4.40
251.75	0.707289	0.711660	3.37
251.85	0.707226	0.710230	2.30
251.95	0.707203	0.709550	1.75
252.05	0.707200	0.709360	1.65
252.15	0.707201	0.712100	3.70
252.25	0.707121	0.712000	3.63

Figure captions

Figure DR1: Paleogeographic map of Pangea during the Early Triassic. The Zal section was located in the equatorial Tethys on the northern margin of the Iranian microcontinent, which formed part of the Cimmeria terranes. After Algeo and Twitchett (2010).

Figure DR2. $^{87}Sr/^{86}Sr$ versus Sr concentration (ppm). This crossplot shows no clear covariation, indicating that the isotopic values of these rocks may be relatively unaltered by diagenesis.

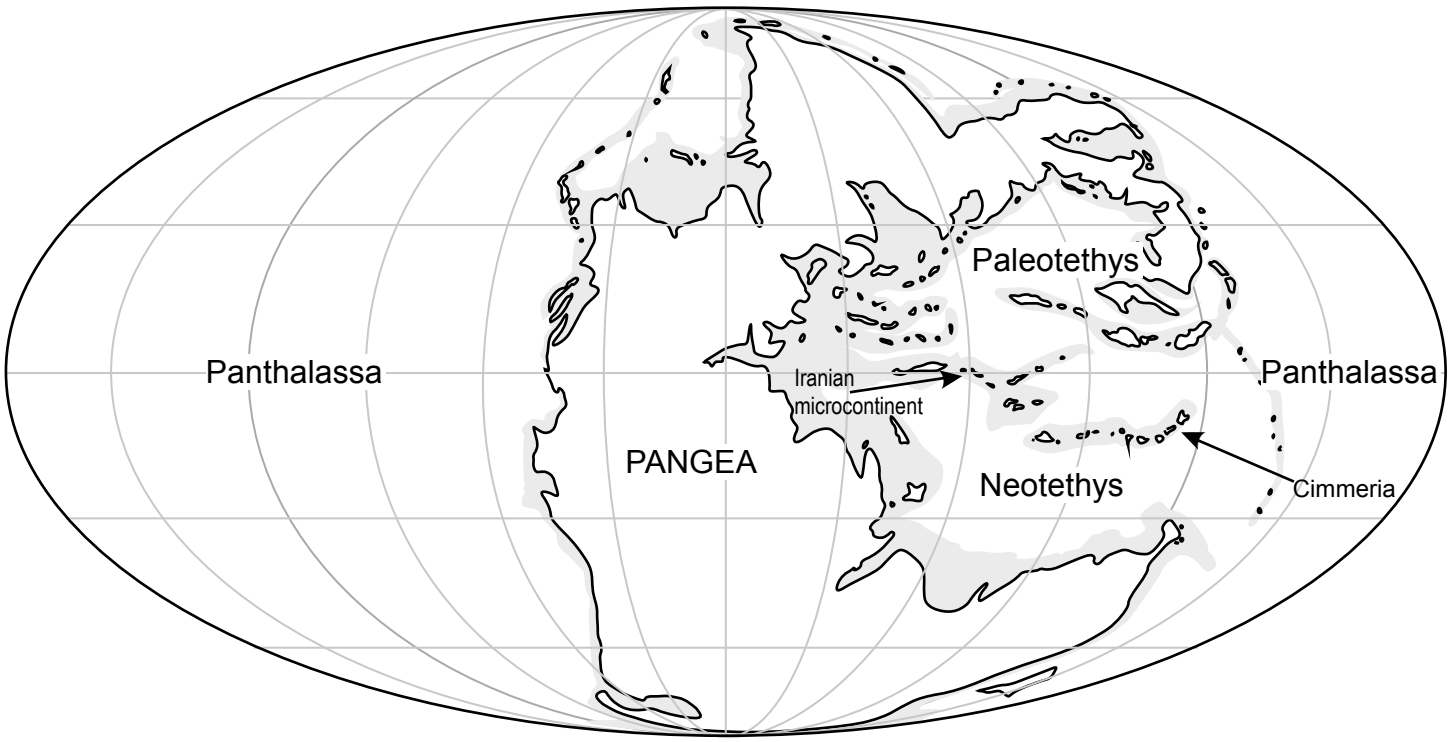

Figure DR1: Paleogeographic map of Pangea during the Early Triassic. The Zal section was located in the equatorial Tethys on the northern margin of the Iranian microcontinent, which formed part of the Cimmeria terranes. After Algeo and Twitchett (2010).

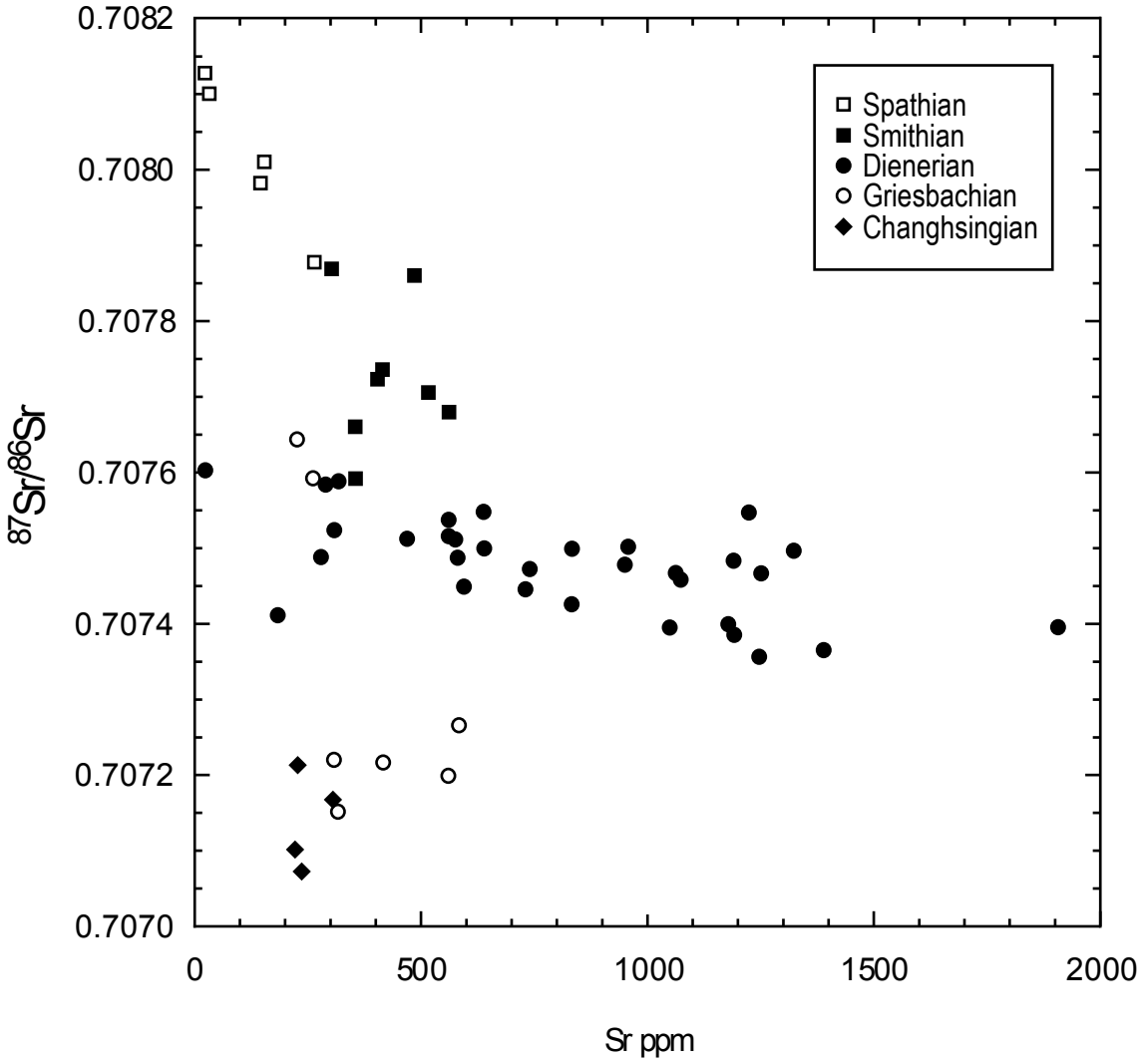

Figure DR2. $^{87}Sr/^{86}Sr$ versus Sr concentration (ppm). This crossplot shows no clear covariation, indicating that the isotopic values of these rocks may be relatively unaltered by diagenesis.